Journal of Instrumentation

SISSA

Radioactive source calibration test of the CMS Hadron Endcap Calorimeter test wedge with Phase I upgrade electronics

To cite this article: S. Chatrchyan *et al* 2017 *JINST* **12** P12034

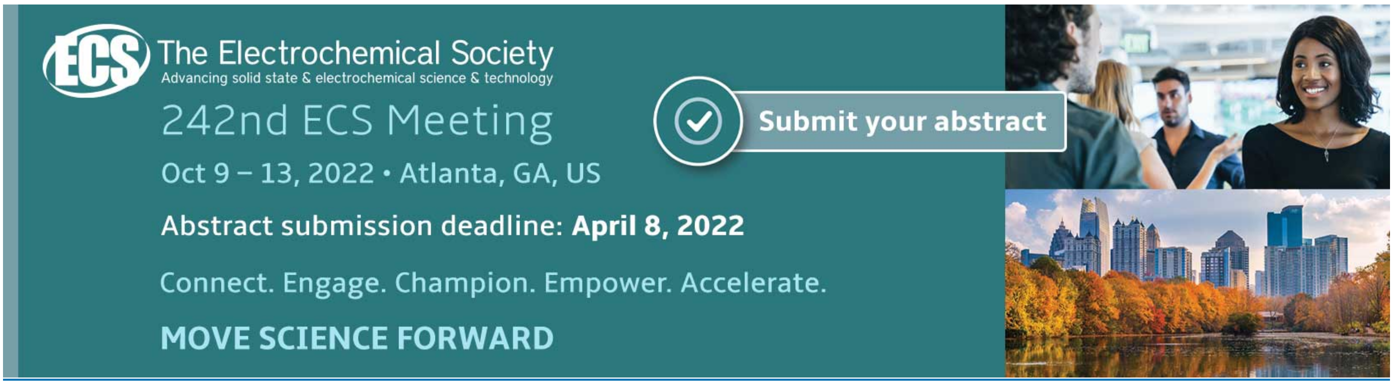

PUBLISHED BY IOP PUBLISHING FOR SISSA MEDIALAB

RECEIVED: *July 26, 2017*
ACCEPTED: *December 6, 2017*
PUBLISHED: *December 22, 2017*

Radioactive source calibration test of the CMS Hadron Endcap Calorimeter test wedge with Phase I upgrade electronics

The CMS HCAL collaboration

E-mail: Burak.Bilki@cern.ch

ABSTRACT: The Phase I upgrade of the CMS Hadron Endcap Calorimeters consists of new photodetectors (Silicon Photomultipliers in place of Hybrid Photo-Diodes) and front-end electronics. The upgrade will eliminate the noise and the calibration drift of the Hybrid Photo-Diodes and enable the mitigation of the radiation damage of the scintillators and the wavelength shifting fibers with a larger spectral acceptance of the Silicon Photomultipliers. The upgrade also includes increased longitudinal segmentation of the calorimeter readout, which allows pile-up mitigation and recalibration due to depth-dependent radiation damage.

As a realistic operational test, the responses of the Hadron Endcap Calorimeter wedges were calibrated with a ^{60}Co radioactive source with upgrade electronics. The test successfully established the procedure for future source calibrations of the Hadron Endcap Calorimeters. Here we describe the instrumentation details and the operational experiences related to the sourcing test.

KEYWORDS: Detector alignment and calibration methods (lasers, sources, particle-beams); Calorimeter methods; Calorimeters

2017 JINST 12 P12034

https://doi.org/10.1088/1748-0221/12/12/P12034

Contents

2017 JINST 12 P12034

1 Introduction

The Compact Muon Solenoid (CMS) is a general-purpose detector designed to run at the highest luminosity provided by the CERN Large Hadron Collider (LHC) [1]. The CMS calorimeters were designed to cleanly detect the diverse signatures of new physics through the measurement of jets and missing transverse energy. The CMS experiment has a 4 T superconducting solenoidal magnet of length 13 m and inner diameter 5.9 m. The barrel and end-cap calorimeters are located inside this magnet.

The hadron endcap calorimeter (HE) is a sampling calorimeter covering the pseudorapidity range $1.3 < |\eta| < 3$. The active medium of the HE is scintillator tiles placed in trays that are inserted between the absorber plates of cartridge brass (70 % Cu and 30 % Zn). The trapezoidal-shaped scintillators are composed of 3.7 mm thick Kuraray SCSN81 or 9.0 mm thick Bicron BC408 for the layer closest to the interaction point, Layer 0. The scintillator tiles are painted white along the narrow edges and placed into a frame to form a tray. This tray, which reads a 10° ϕ sector of the detector, is called a megatile. Two megatiles form a wedge of the calorimeter. The total number of trays for both HE calorimeters is 1368 in 36 wedges.

The scintillation light is collected by 0.94 mm diameter wavelength shifting (WLS) fibers, inserted in machined groves near the periphery of the scintillator tiles. The ends of the WLS fibers are machined with a diamond fly cutter, and one end is aluminized by sputtering to increase the light collection. The other end is spliced to a 0.94 mm diameter clear fiber, which is glued in a custom made optical connector. The readout boxes (RBXs), which contain the photodetectors and front-end electronics, are located at the back of the calorimeter, near the edges. Multipixel hybrid photodiodes (HPDs) are used as photodetectors. Figure 1 shows a picture of the HE (left) and a sketch of the longitudinal and transverse segmentation (right).

A radioactive source calibration system, using a ^{60}Co source, exists in HE. In this system, the radioactive source on the tip of a wire moves in stainless steel tubes embedded in the megatiles. The system allows driving of the radioactive source to every single tile in HE. The radioactive source is not stored on the detector during operations. Instead, the radioactive source calibration is performed whenever necessary and possible. Identical calibration system exists for the HE test wedge, which will be described in detail below.

Further information about HE can be found in reference [2].

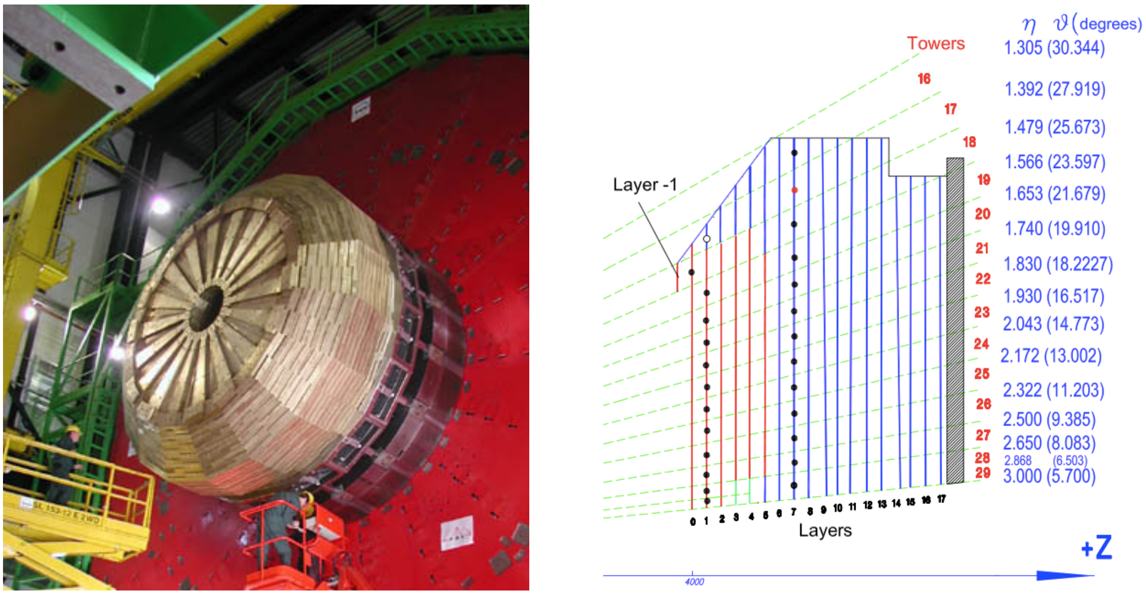

Figure 1. A picture of the HE (left) and a sketch of the longitudinal and transverse segmentation (right, not to scale). Within the same η tower, longitudinal sections with identical colors (red, green or blue) belong to the same calorimeter readout channel. The dots denote the light injection points for the laser calibration system.

The Phase I upgrade of HE consists of new photodetectors (Silicon photomultipliers — SiPMs) and upgraded front-end electronics (QIE11 — Charge Integration and Encoding [3]). The upgrade will allow the elimination of the high amplitude noise and drifting response of the HPDs, at the same time enabling the mitigation of the radiation damage of the scintillators and the wavelength shifting fibers with the larger spectral acceptance of the SiPMs. The upgrade will also have increased longitudinal segmentation of the readout, which is beneficial for pile-up mitigation and recalibration to correct for depth-dependent radiation damage [4].

As a realistic operational test, the responses of the Hadron Endcap Calorimeter test wedges, permanently located in the CERN H2 beam line in the SPS North area [5], were calibrated with a ^{60}Co radioactive source with upgrade electronics. Here we describe the nature of the test, discuss the results and operational experience.

2 Description of the test setup and the data acquisition

The source calibration test was performed with two of the ϕ sectors of one of the permanently installed wedges in the CERN H2 test beam area. Figure 2 shows a picture of the test area. Test segments of the CMS hadron endcap, barrel and outer calorimeters are installed on a motion table which allows precision alignment of the detectors with respect to the test beam. During the source calibration test, there was no beam in the test area.

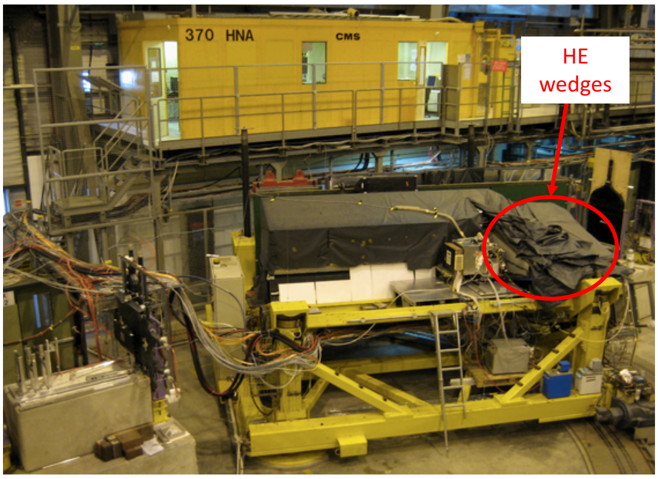

Figure 2. Picture of the H2 test area showing the location of the HE wedges on the motion table.

Figure 3 shows a sketch of the HE test megatile. The megatile consists of 16 scintillator tiles, all of which have sigma-shaped grooves machined on the surface near the periphery of the tiles. The WLS fibers inserted in these grooves are then individually coupled to clear fibers which transport the light to the readout modules housing the 96 SiPMs. Only two of the four available slots of readout modules in the HE RBX were used in this test. The RBX also houses the control and QIE11-based front-end electronics which are connected to the back-end electronics in the control room via control and data fibers. The back-end electronics is the current μTCA-based system of the CMS HE [6]. Figure 3 also shows the locations of the source tubes inside the megatile as red tubes. The source tube along $\phi = 5$ sector goes across six scintillator tiles, and the one along ϕ=6 sector goes across ten tiles. Also shown are the η indices from 16 to 25. Although structurally and functionally identical, the geometry of the test megatile differs from the actual megatiles of the HE. In the actual HE megatiles, $\eta = 21$ tile has a single ϕ sector and the η segmentation goes up to 29 instead of 25. Because the test wedges have been connected and disconnected as part of ten years of testing, the performance of the optical connections is expected to have degraded to some extent. Therefore, it was not intended to obtain an absolute calibration as a result of this test. Up to 13 megatile layers were tested with the radioactive source. Various consecutive layers in the wedge were combined to form calorimeter towers. The towers with η indices between 16 and 21 cover 5° in ϕ and those with η indices between 22 and 25 cover 10° angles.

Figure 4 shows a picture of the radioactive source driver, the indexer and the source tubes. The radioactive source is loaded at the end of the source wire that is wound around the source driver reel. The source wire is made of stainless steel and has an inner and outer diameter of 0.406 mm and 0.711 mm respectively. The radioactive source, in the shape of a cylinder with 1 mm diameter and 100 μm thickness, is inserted into the end of the wire and held in place by a fine steel piano wire. The outer source wire and inner piano wire are then crimped together at the back end in order to fix the position of the radioactive source. The activity of the ^{60}Co source used in this test was

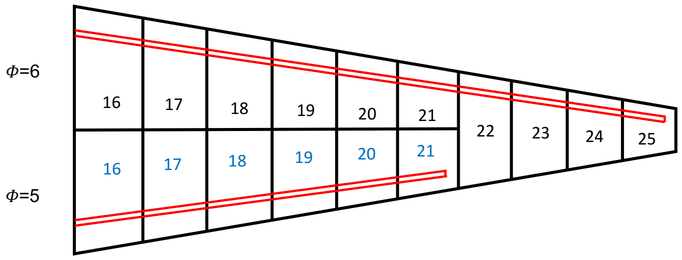

Figure 3. Sketch of the HE test megatile (not to scale). ϕ sectors, η indices (numbers in black and blue) and the approximate locations of the source tubes (red tubes) are indicated.

46.88 MBq. The same source is used to calibrate the actual HE.

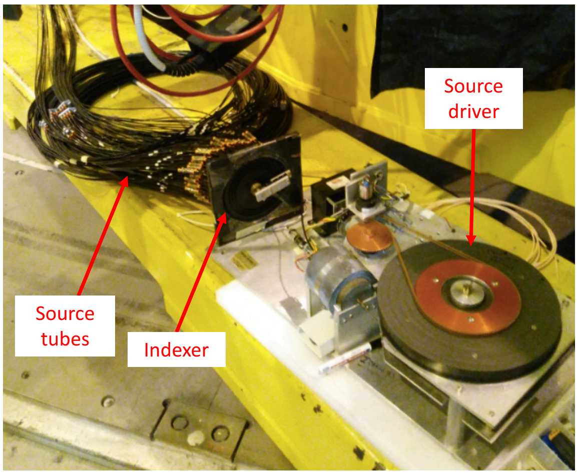

Figure 4. Picture of the source driver, the indexer and the external source tubes.

A polycarbonate reel, belt driven by a DC reversible electric motor, is used to insert or retract the source wire into or out of the calorimeter source tubes. The calorimeter source tubes are coupled to acetal plastic tubing to mediate the transfer of the source wire from the source driver into the calorimeter. The transition between the plastic tube and the stainless steel source tube inside the calorimeter typically involves small-angle conical holes in brass that channel the source wire to the calorimeter source tube.

The driver system also contains an additional electric motor that functions to select the source tube into which to direct the source wire, an action referred to as indexing. The position of the radioactive source, relative to the source driver and referred to as the reel position, is provided by an optical rotary encoder read out by industrial batch counters. The speeds at which the radioactive source may be inserted or retracted by the driver are between 1 and 12 cm/s.

The data acquisition system continuously records the location of the radioactive source and the data from the 96 SiPMs. The data from the SiPMs are histograms of ADC counts for a predefined number of time samples (TS) of 25 ns length each (40 MHz, which is the LHC frequency). The system can also take pedestal and LED data, where the data from the SiPMs are randomly read out for the former, and the data taking is initiated by the firing of LED light into the SiPMs for the latter. In both of these cases, the data is ten consecutive time samples. Due to the ongoing firmware development of the front-end electronics at the time of this test, the data from the first time sample was not available.

3 Calibration of the SiPMs

For the calibration of the SiPMs, dedicated pedestal data is used. The SiPMs had 15 μm pitch pixels in a 2.8 mm diameter effective photosensitive area, and were made by Hamamatsu [7]. They were operated at a stable temperature of 18 $^\circ C$ provided by peltier cooling. The dark current rate for these SiPMs were approximately 1 MHz. SiPM bias voltages were turned on and were also stable during the pedestal data taking. Therefore, a sufficiently large integration time window in the pedestal data would contain up to a few photon pulses. One can then extract the charge per detected photon (defined as the gain of the SiPM hereafter) from the distribution of the integrated charges.

For each time sample, the raw ADC values read out from the QIE11 front-end cards are converted into corresponding charge values using the conversion tables specific to the QIE11 chips [3]. Of the nine available consecutive time samples, four are used to form the 100-ns integration window. A selection on the sum of the charges in the neighboring time samples is imposed in order to prevent transients and have the entire single or multiple photon pulses contained within the integration window. The integration and the transients windows are shown in figure 5 (left) as red and grey shaded areas. Figure 5 (right) shows the distribution of the transient window charges for one SiPM. The selection is applied at the charge value where the Gaussian fit falls by three orders of magnitude of the peak value. This selection is determined for each SiPM separately. For this particular SiPM, approximately 5 % of events have partial avalanches in the transients window and are described by the tail of the distribution shown in figure 5 (right). The integration window for each pedestal event is identified using the first set of six consecutive time samples satisfying this selection.

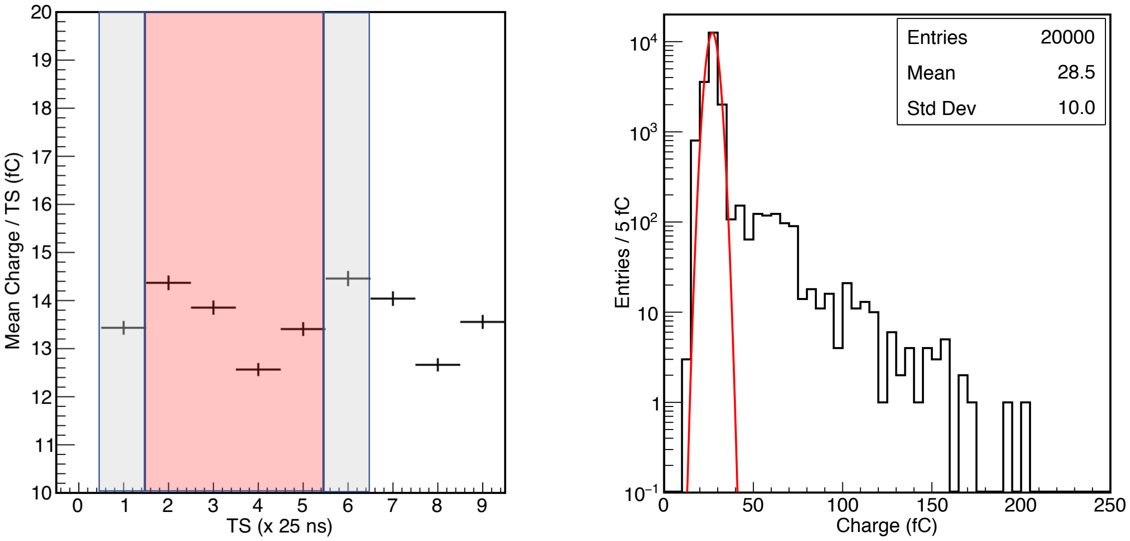

Figure 5. Integration (red) and transients (grey) windows demonstrated on the average of the pedestal signals (left) and the transients window charges for a particular SiPM (right). Also shown is the Gaussian fit which was used to determine the maximum signal allowed in the transients window (right).

Figure 6 shows the integration window charge spectrum of this SiPM, using the same dedicated pedestal data. Pedestal and the one, two and three photon peaks are clearly measurable. Four, five and six photon signatures are also observable. The spectrum is fit with a single function:

$$f(x) = \sum_{i=0}^{N_{\text{peaks}}-1} A_i e^{-\frac{1}{2}\left(\frac{x-\mu_i}{\sigma_i}\right)^2} \tag{3.1}$$

where $\mu_i = \mu_0 + iG$. The function is basically a sum of Gaussians with independent weights A_i and widths σ_i; and means μ_i are parametrized as a function of the pedestal mean μ_0, the peak id i and the SiPM gain G (charge generated by a single photon). The range of the fit is such that all the photon peaks are larger than 1/1000 of the pedestal peak. Figure 6 shows all the parameters obtained for this particular SiPM. The gain of the SiPM is a parameter of this fit function.

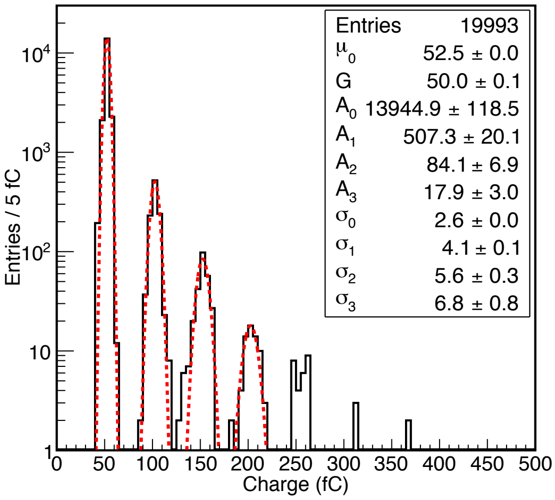

Figure 6. Example of integration window charge spectrum of the SiPMs. Also shown is the combined fit to the spectrum.

During the radioactive source test, the SiPM bias voltages were adjusted for two gain values of 50 fC and 40 fC. Figure 7 shows the measured gain values for the 50 fC setting (blue) and 40 fC setting (red) for all SiPMs. Also shown are the constant fits to the gain values yielding 50.40 ± 0.01 fC and 40.71 ± 0.01 fC respectively. The uniformity of the gains is sufficient for the purposes of the test. These gain values are used to convert the charge values calculated in the sourcing test into number of photoelectrons as described in the next section.

4 Analysis of the radioactive source calibration data

The radioactive source calibration data is a set of histograms periodically accumulated by the back-end electronics for each readout channel in ADC units. Also recorded is the position of the radioactive source inside the megatile. Individual histograms are first converted from ADC units to charge in fC. After the pedestal subtraction, the average charge values of these histograms are converted to number of photoelectrons using the previously obtained gain values. It should be noted

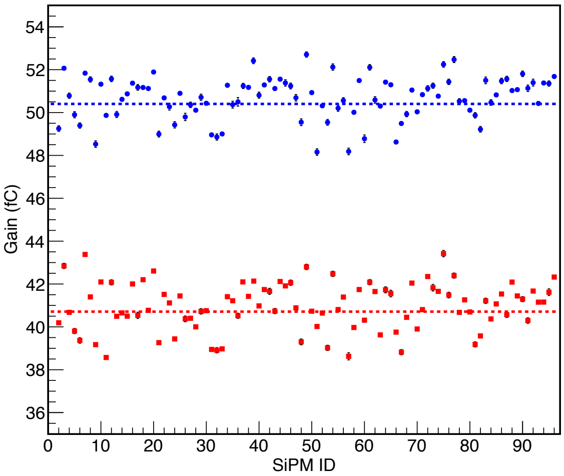

Figure 7. Measured gain values for 50 fC (blue) and 40 fC (red) settings and the corresponding fits to a constant value.

here that this is a numerical conversion to equalize the reponses of the SiPMs and not an actual calculation of the number of photoelectrons. Each bin of the histogram is an integral for 25 ns (instead of 100 ns in the gain calculation) and the signal pulse is not entirely contained in this 25-ns window.

Figure 8 shows the response profiles for $\phi = 5$ (left) and $\phi = 6$ (right) sectors for layers 9 and 8 respectively. The boundaries of the tiles are clearly distinguishable. The profiles are precise enough to calculate the longitudinal size of the tiles as seen by the radioactive source.

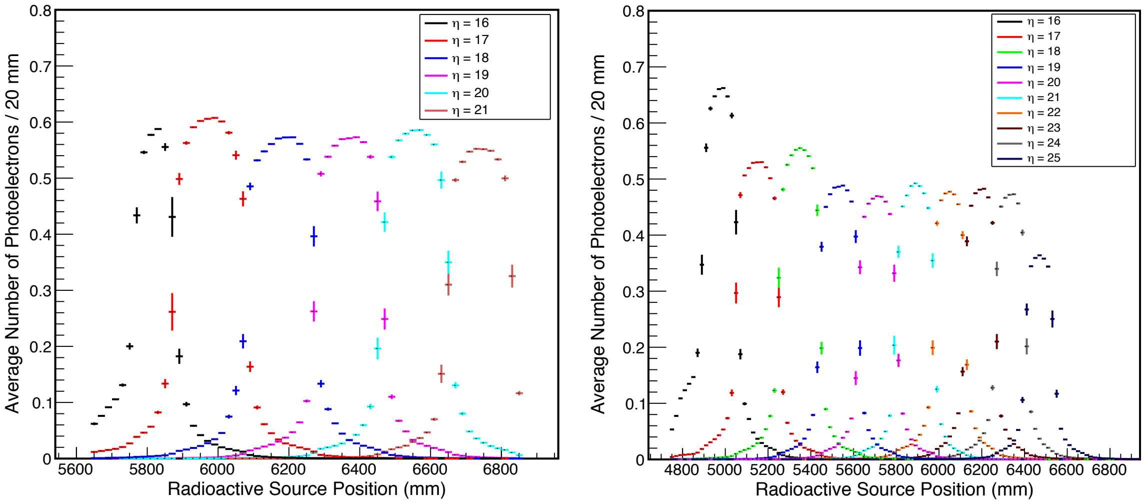

Figure 8. Response profiles for $\phi = 5$ layer 9 (left) and $\phi = 6$ layer 8 (right) sections.

In order to obtain an average response value to the radioactive source, the spectrum of the number of photoelectrons is extracted for each signal channel with a zero suppression at 0.07 photoelectrons. This zero suppression value is selected to be slightly above the usual pedestal fluctuations measured of around 0.05 photoelectrons (2.6 fC or σ_0 in figure 6). Figure 9 shows this spectrum for the signal channel of the $\phi = 5$, $\eta = 20$ layer 9 tile. The spectrum is fit to a Gaussian function with a variable width defined as

$$f(x) = N_0 e^{-\frac{1}{2}\left(\frac{x-\mu}{\sigma(x)}\right)^2} \tag{4.1}$$

with

$$\sigma(x) = \begin{cases} \sigma_0 + \alpha_1 (\mu - x)^{\beta_1} & \text{for } x < \mu \\ \sigma_0 + \alpha_2 (x - \mu)^{\beta_2} & \text{for } x \geq \mu \end{cases} \tag{4.2}$$

where N_0 is the weight, μ is the mean, σ_0 is the central width, α_1, β_1 and α_2, β_2 are the parameters defining the varying width to the left and right of the mean respectively [8]. As long as sufficient statistics is present in the distributions, the fits are successful in describing the spectra. The statistics is determined mainly by the speed of the radioactive source inside the megatile, which can be adjusted as a simple parameter in the data acquisition and control system, and will be discussed further below.

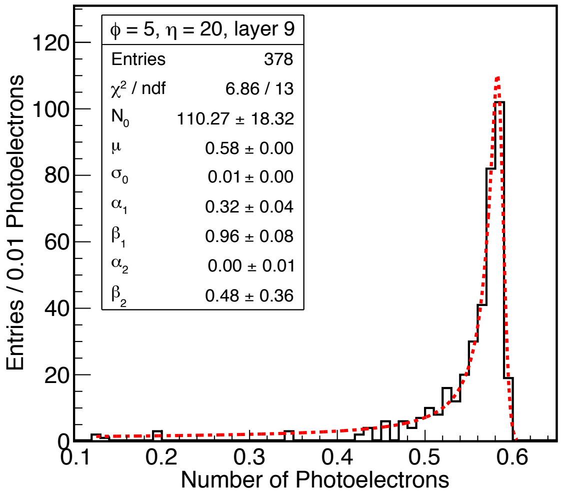

Figure 9. Photoelectron spectrum for the signal channel of $\phi = 5$, $\eta = 20$ layer 9 tile. The spectrum is fit to a Gaussian function with a variable width defined in the text.

5 Results

Following the basic electronics-detector mapping test and calibration, various measurements were performed. The efficiency of radioactive source tests in identifying possible issues in the optical paths as well as establishing the scintillating tile aging and radiation damage was studied by comparing the signals from different layers that form the same physical detector tower and are read out by the same SiPM. Figure 10 shows the responses measured in layers 1 and 2 (left), and layers 7 and 8 (right) when the radioactive source was moving in $\phi = 5$ sector. The error bars are smaller than the size of the marker points. Standard errors are calculated for the averages. Layers 7 and 8 show minimal deviation in response to the radioactive source. The overall decreasing trend towards higher η values is due to the decreasing lateral sizes of the tiles. No attempt was made to correct for this effect in this study. The responses in layers 1 and 2 on the other hand show significant (more than 15 %) deviation in $\eta = 18$ tower. The major reason is that these layers are the most upstream

2017 JINST 12 P12034

layers in the stack and have seen several physical interventions over the course of several years. The sourcing test can successfully identify such potential problems at the per tile level.

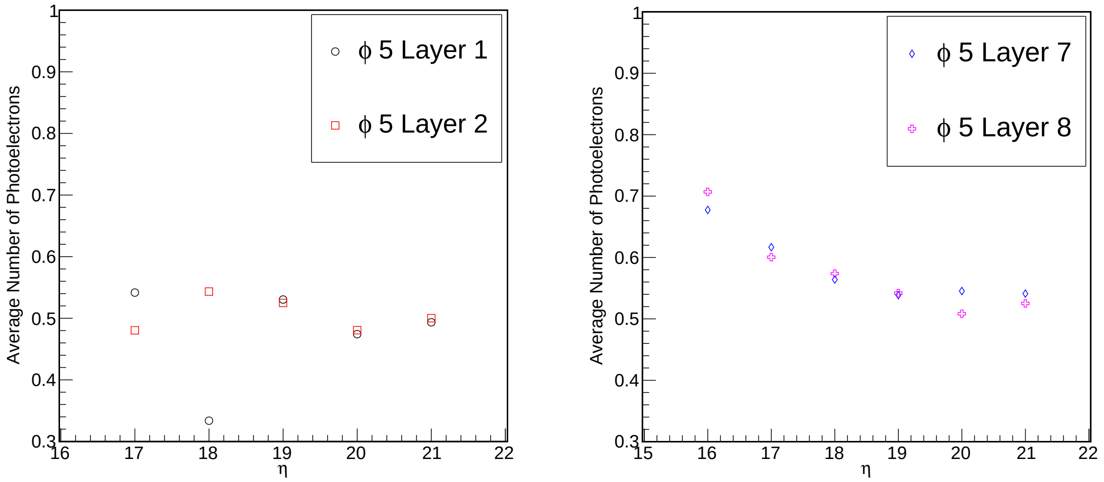

Figure 10. Radioactive source response of layers 1 and 2 (left) and layers 7 and 8 (right) when the radioactive source was moving in $\phi = 5$ sector. Each η value in the panels is a different calorimeter tower. Identical towers in left or right panel are read out with identical SiPMs.

Figure 11 shows a comparison of the responses for layers 7 and 8 (left), and layers 10 and 12 (right) for the $\phi = 6$ sector. All tiles have responses around 0.5 photoelectrons and the variation of the response as a function of the tile size is within expectations. The deviations of the tile signals between layers 7 and 8 and between layers 10 and 12 are within 15 %. The quality of the results obtained indicates that with periodic radioactive source calibration of the actual HE detector during the Phase I era, the combined performance degradation of the tiles and the optical path due to radiation can be precisely measured and the response can be corrected.

The $\phi = 5$ sector was also subjected to further testing of the radioactive source calibration. The first of these tests was the dependence of the source response on the source speed inside the megatile. As the source moves faster, the number of histograms and hence the number of data points in the photoelectron spectra (e.g. figure 9) are reduced. Therefore, the fit procedure may become problematic. The default source wire speed in these tests was 2 cm/s. $\phi = 5$ sector was also tested at 1 cm/s to search for any improvements in the results. Figure 12 (left) shows the response at 2 cm/s (black) and 1 cm/s (red) source wire speeds as well as the deviations per tile for the tiles in layer 6 in $\phi = 5$ sector. The deviation between these two speed settings is minimal. The overall statistics and the quality of the fits of the photoelectron spectra improve as expected. Since larger speeds are desired for practical purposes, it can be concluded that the final results are not affected by increasing the speed of the source wire by a factor of two, from 1 cm/s to 2 cm/s. For the default setting of 2 cm/s, the radioactive source calibration of one wedge takes around 40 minutes. With the information obtained in these tests, the time and effort needed to set up the calibration hardware and to perform the operations for HE were estimated with sufficient accuracy.

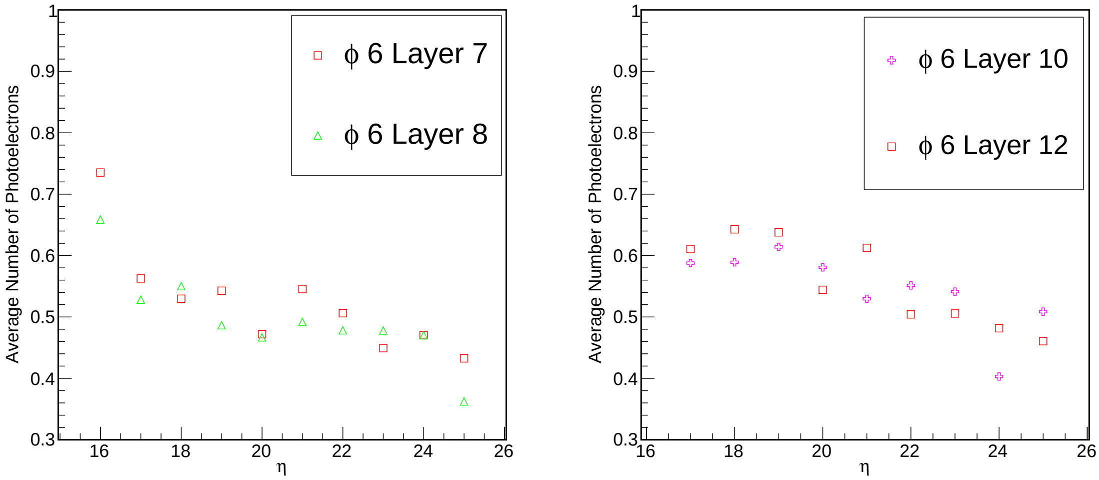

Figure 11. Radioactive source response of layers 7 and 8 (left) and layers 10 and 12 (right) when the radioactive source was moving in $\phi = 6$ sector. Each η value in the panels is a different calorimeter tower. Identical towers in left or right panel are read out with identical SiPMs.

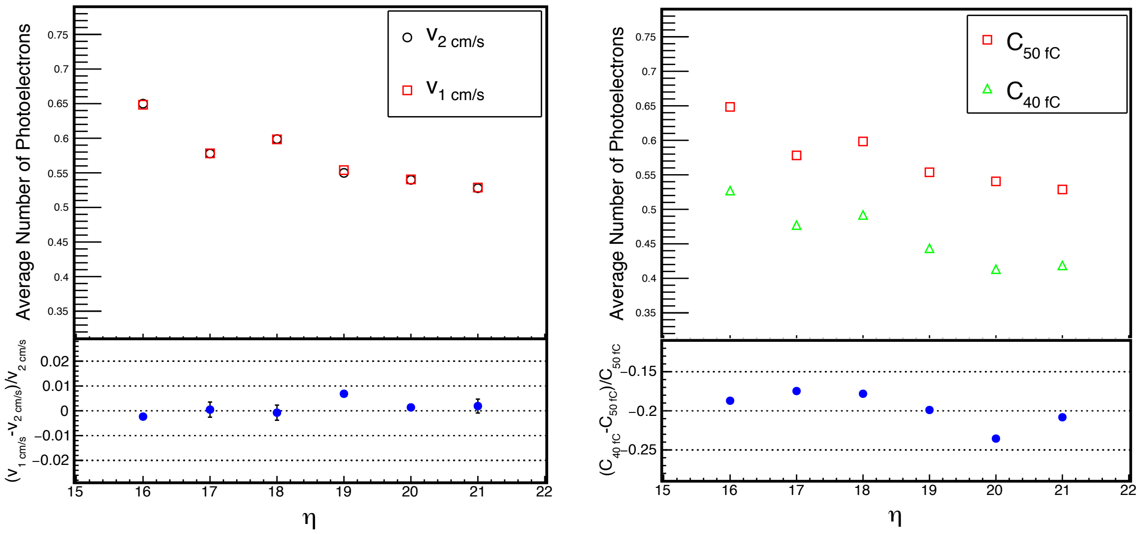

Figure 12. Source response of the $\phi = 5$ sector tiles at layer 6 for the source wire speeds of 2 cm/s (black) and 1 cm/s (red) (left); and for the SiPM gain settings of 50 fC (red) and 40 fC (green) (right) together with their per tile deviations (lower panels).

Figure 12 (right) shows the response of the $\phi = 5$ sector tiles with different bias voltage settings of the SiPMs. The red squares are for the default setting of 50 fC gain, and the green triangles are for the gain setting of 40 fC. Also shown is the deviation per tile in the lower panel. As expected, the response at 40 fC gain is on average 20 % lower than the reponse at 50 fC gain. It can be concluded that the radioactive source calibration results can be translated to a different operating gain of the SiPMs within 5 % accuracy. This information would be useful in the long term in identifying the systematics of the radioactive source calibration due to e.g. the radiation damage to the SiPMs.

6 Conclusions

The test described here validates the radioactive source calibration operations of the actual CMS Hadron Endcap calorimeter wedges several months ahead of the actual Hadron Endcap Calorimeters source calibration campaign during the Extended Year End Technical Stop of 2016-2017. The test allows the estimation of the time and effort needed for the actual source calibration campaign. It provides insight about the effect of the source wire speed and the SiPM calibration on the quality and quantity of the data.

Various techniques were developed for the analysis of the data. The analysis methods developed during the test combine the features of fast calibration of large-scale SiPM arrays and fast extraction of the radioactive source response of several thousands of scintillator tiles, and were successfully implemented at the actual sourcing campaign. This test also forms the basis of the techniques to be implemented in the radioactive source calibration of the Phase I upgrade of the Hadron Endcap Calorimeters during Year End Technical Stop 2017-2018. The test validates the automated radioactive source calibration concept for scintillator-based calorimeters and provides insight on the applicability of this concept to large-scale detector systems.

References

[1] CMS collaboration, *The CMS experiment at the CERN LHC*, 2008 *JINST* **3** S08004, pg. 145.

[2] CMS HCAL collaboration, *Design, performance and calibration of CMS Hadron Endcap Calorimeters*, CMS-NOTE-2008-010, CERN, Geneva Switzerland, (2008).

[3] D. Hare, A. Baumbaugh, L.D. Monte, J. Freeman, J. Hirschauer, E. Hughes et al., *First large volume characterization of the QIE*10/11 *custom front-end integrated circuits*, 2016 *JINST* **11** C02052.

[4] CMS HCAL collaboration, *Dose rate effects in the radiation damage of the plastic scintillators of the CMS Hadron Endcap Calorimeter*, 2016 *JINST* **11** T10004 [`arXiv:1608.07267`].

[5] *H2 beam line webpage*, http://sba.web.cern.ch/sba/BeamsAndAreas/resultbeam.asp?beamline=H2.

[6] M.O. Sahin, U. Behrens, A. Campbell, I. Martens, I.A. Melzer-Pellmann and P. Saxena, *The CMS hadron calorimeter detector control system upgrade*, 2015 *JINST* **10** C04029.

[7] *Hamamatsu webpage*, http://www.hamamatsu.com/.

[8] I. Ambats, J. Dawson, M. Derrick, S. Magill, B. Musgrave, J. Repond et al., *Cosmic ray tests of the ZEUS barrel calorimeter modules*, *Nucl. Instrum. Meth.* **A 320** (1992) 161.

The CMS HCAL collaboration

Yerevan Physics Institute, Yerevan, Armenia
S. Chatrchyan, A.M. Sirunyan, A. Tumasyan

National Centre for Particle and High Energy Physics, Minsk, Belarus
A. Litomin, V. Mossolov, N. Shumeiko[†]

Universiteit Antwerpen, Antwerpen, Belgium
M. Van De Klundert, H. Van Haevermaet, P. Van Mechelen, A. Van Spilbeeck

Centro Brasileiro de Pesquisas Fisicas, Rio de Janeiro, Brazil
G.A. Alves, W.L. Aldá Júnior, C. Hensel

Universidade do Estado do Rio de Janeiro, Rio de Janeiro, Brazil
W. Carvalho, J. Chinellato, C. De Oliveira Martins, D. Matos Figueiredo, C. Mora Herrera, H. Nogima, W.L. Prado Da Silva, E.J. Tonelli Manganote, A. Vilela Pereira

Charles University, Prague, Czech Republic
M. Finger, M. Finger Jr., A. Kveton, J. Tomsa

Institute of High Energy Physics and Informatization, Tbilisi State University, Tbilisi, Georgia
G. Adamov, Z. Tsamalaidze[1]

Deutsches Elektronen-Synchrotron, Hamburg, Germany
U. Behrens, K. Borras, A. Campbell, F. Costanza, P. Gunnellini, A. Lobanov, I.-A. Melzer-Pellmann, C. Muhl, B. Roland, M. Sahin, P. Saxena

Indian Institute of Science Education and Research, Pune, India
V. Hegde, K. Kothekar, S. Pandey, S. Sharma

Panjab University, Chandigarh, India
S.B. Beri, B. Bhawandeep, R. Chawla, A. Kalsi, A. Kaur, M. Kaur, G. Walia

Saha Institute of Nuclear Physics, Kolkata, India
S. Bhattacharya, S. Ghosh, S. Nandan, A. Purohit, M. Sharan

Tata Institute of Fundamental Research-B, Mumbai, India
S. Banerjee, S. Bhattacharya, S. Chatterjee, P. Das, M. Guchait, S. Jain, S. Kumar, M. Maity, G. Majumder, K. Mazumdar, M. Patil, T. Sarkar

Vilnius University, Vilnius, Lithuania
A. Juodagalvis

Joint Institute for Nuclear Research, Dubna, Russia
S. Afanasiev, P. Bunin, Y. Ershov, I. Golutvin, A. Malakhov, P. Moisenz[†], V. Smirnov, A. Zarubin

National Research Nuclear University Moscow Engineering Physics Institute, Moscow, Russia
M. Chadeeva, R. Chistov, M. Danilov, E. Popova, V. Rusinov

Institute for Nuclear Research, Moscow, Russia
Yu. Andreev, A. Dermenev, A. Karneyeu, N. Krasnikov, D. Tlisov, A. Toropin

Institute for Theoretical and Experimental Physics, Moscow, Russia

V. Epshteyn, V. Gavrilov, N. Lychkovskaya, V. Popov, I. Pozdnyakov, G. Safronov, M. Toms, A. Zhokin

Moscow State University, Moscow, Russia

A. Baskakov, A. Belyaev, E. Boos, M. Dubinin[2], L. Dudko, A. Ershov, A. Gribushin, A. Kaminskiy, V. Klyukhin, O. Kodolova, I. Lokhtin, I. Miagkov, S. Obraztsov, S. Petrushanko, V. Savrin, A. Snigirev

P.N. Lebedev Physical Institute, Moscow, Russia

V. Andreev, M. Azarkin, I. Dremin, M. Kirakosyan, A. Leonidov, A. Terkulov

State Research Center of Russian Federation, Institute for High Energy Physics, Protvino, Russia

S. Bitioukov, D. Elumakhov, A. Kalinin, V. Krychkine, P. Mandrik, V. Petrov, R. Ryutin, A. Sobol, S. Troshin, A. Volkov

Kyungpook National University, Daegu, South Korea

S. Sekmen

CERN, European Organization for Nuclear Research, Geneva, Switzerland

P. Rumerio[3]

Cukurova University, Adana, Turkey

A. Adiguzel, N. Bakirci[4], S. Cerci[5], S. Damarseckin, Z.S. Demiroglu, F. Dölek, C. Dozen, I. Dumanoglu, E. Eskut, S. Girgis, G. Gokbulut, Y. Guler, I. Hos, E.E. Kangal, O. Kara, A. Kayis Topaksu, C. Işik, U. Kiminsu, M. Oglakci, G. Onengut, K. Ozdemir[6], S. Ozturk[4], A. Polatoz, D. Sunar Cerci[5], B. Tali[5], H. Topakli[4], S. Turkcapar, I.S. Zorbakir, C. Zorbilmez

Middle East Technical University, Physics Department, Ankara, Turkey

B. Bilin, B. Isildak, G. Karapinar, A. Murat Guler, K. Ocalan[7], M. Yalvac, M. Zeyrek

Bogazici University, Istanbul, Turkey

I.O. Atakisi[8], E. Gülmez, M. Kaya[8], O. Kaya[9], O.K. Koseyan, O. Ozcelik[10], S. Ozkorucuklu[11], S. Tekten[9], E.A. Yetkin[12], T. Yetkin[13]

Istanbul Technical University, Istanbul, Turkey

K. Cankocak, S. Sen[14]

Institute for Scintillation Materials of National Academy of Science of Ukraine, Kharkov, Ukraine

A. Boyarintsev, B. Grynyov

National Scientific Center, Kharkov Institute of Physics and Technology, Kharkov, Ukraine

L. Levchuk, V. Popov, P. Sorokin

University of Bristol, Bristol, United Kingdom

H. Flacher

Baylor University, Waco, U.S.A.

A. Borzou, K. Call, J. Dittmann, K. Hatakeyama, H. Liu, N. Pastika

The University of Alabama, Tuscaloosa, U.S.A.

A. Buccilli, S.I. Cooper, C. Henderson, C. West

Boston University, Boston, U.S.A.

D. Arcaro, D. Gastler, E. Hazen, J. Rohlf, L. Sulak, S. Wu, D. Zou

Brown University, Providence, U.S.A.

J. Hakala, U. Heintz, K.H.M. Kwok, E. Laird, G. Landsberg, Z. Mao, D.R. Yu

University of California, Riverside, Riverside, U.S.A.

J.W. Gary, S.M. Ghiasi Shirazi, F. Lacroix, O.R. Long, H. Wei

University of California, Santa Barbara, Santa Barbara, U.S.A.

R. Bhandari, R. Heller, D. Stuart, J.H. Yoo

California Institute of Technology, Pasadena, U.S.A.

Y. Chen, J. Duarte, J.M. Lawhorn, T. Nguyen, M. Spiropulu

Fairfield University, Fairfield, U.S.A.

D. Winn

Fermi National Accelerator Laboratory, Batavia, U.S.A.

S. Abdullin, A. Apresyan, A. Apyan, S. Banerjee, F. Chlebana, J. Freeman, D. Green, D. Hare, J. Hirschauer, U. Joshi, D. Lincoln, S. Los, K. Pedro, W.J. Spalding, N. Strobbe, S. Tkaczyk, A. Whitbeck

Florida International University, Miami, U.S.A.

S. Linn, P. Markowitz, G. Martinez

Florida State University, Tallahassee, U.S.A.

M. Bertoldi, S. Hagopian, V. Hagopian, T. Kolberg

Florida Institute of Technology, Melbourne, U.S.A.

M.M. Baarmand, D. Noonan, T. Roy, F. Yumiceva

The University of Iowa, Iowa City, U.S.A.

B. Bilki[15,22], W. Clarida, P. Debbins, K. Dilsiz, S. Durgut, R.P. Gandrajula, M. Haytmyradov, V. Khristenko, J.-P. Merlo, H. Mermerkaya[16], A. Mestvirishvili, M. Miller, A. Moeller, J. Nachtman, H. Ogul, Y. Onel, F. Ozok[10], A. Penzo, I. Schmidt, C. Snyder, D. Southwick, E. Tiras, K. Yi

The University of Kansas, Lawrence, U.S.A.

A. Al-bataineh, J. Bowen, J. Castle, W. McBrayer, M. Murray, Q. Wang

Kansas State University, Manhattan, U.S.A.

K. Kaadze, Y. Maravin, A. Mohammadi, L.K. Saini

University of Maryland, College Park, U.S.A.

A. Baden, A. Belloni, J.D. Calderon[17], S.C. Eno, Y. B. Feng, C. Ferraioli, T. Grassi, N.J. Hadley, G-Y Jeng, R.G. Kellogg, J. Kunkle, A. Mignerey, F. Ricci-Tam, Y.H. Shin, A. Skuja, Z.S. Yang, Y. Yao[18]

Massachusetts Institute of Technology, Cambridge, U.S.A.

S. Brandt, M. D'Alfonso, M. Hu, M. Klute, X. Niu

University of Minnesota, Minneapolis, U.S.A.

R.M. Chatterjee, A. Evans, E. Frahm, Y. Kubota, Z. Lesko, J. Mans, N. Ruckstuhl

University of Notre Dame, Notre Dame, U.S.A.

A. Heering, D.J. Karmgard, Y. Musienko[19], R. Ruchti, M. Wayne

Princeton University, Princeton, U.S.A.

A.D. Benaglia[20], T. Medvedeva[21], K. Mei, C. Tully

University of Rochester, Rochester, U.S.A.

A. Bodek, P. de Barbaro, M. Galanti, A. Garcia-Bellido, A. Khukhunaishvili, K.H. Lo, D. Vishnevskiy, M. Zielinski

Rutgers, the State University of New Jersey, Piscataway, U.S.A.

A. Agapitos, M. Amouzegar, J.P. Chou, E. Hughes, H. Saka, D. Sheffield

Texas Tech University, Lubbock, U.S.A.

N. Akchurin, J. Damgov, F. De Guio, P.R. Dudero, J. Faulkner, E. Gurpinar, S. Kunori, K. Lamichhane, S.W. Lee, T. Libeiro, T. Mengke, S. Muthumuni, S. Undleeb, I. Volobouev, Z. Wang

University of Virginia, Charlottesville, U.S.A.

S. Goadhouse, R. Hirosky, Y. Wang

†: Deceased
1: Also at Joint Institute for Nuclear Research, Dubna, Russia
2: Also at California Institute of Technology, Pasadena, U.S.A.
3: Also at The University of Alabama, Tuscaloosa, U.S.A.
4: Also at Gaziosmanpasa University, Tokat, Turkey
5: Also at Adiyaman University, Adiyaman, Turkey
6: Also at Piri Reis University, Istanbul, Turkey
7: Also at Necmettin Erbakan University, Konya, Turkey
8: Also at Marmara University, Istanbul, Turkey
9: Also at Kafkas University, Kars, Turkey
10: Also at Mimar Sinan University, Istanbul, Turkey
11: Also at Istanbul University, Istanbul, Turkey
12: Also at Istanbul Bilgi University, Istanbul, Turkey
13: Also at Yildiz Technical University, Istanbul, Turkey
14: Also at Hacettepe University, Ankara, Turkey
15: Also at Beykent University, Istanbul, Turkey
16: Also at Erzincan University, Erzincan, Turkey

17: Now at NOAA, National Oceanic and Atmospheric Administration, U.S.A.
18: Now at University of California, Davis, Davis, U.S.A.
19: Also at Institute for Nuclear Research, Moscow, Russia
20: Now at INFN Sezione di Milano-Bicocca, Milano, Italy
21: Now at CERN, European Organization for Nuclear Research, Geneva, Switzerland
22: Corresponding author